ADVANCED FUNCTIONAL MATERIALS
www.afm-journal.de

Tailoring Ordered Mesoporous Titania Films via Introducing Germanium Nanocrystals for Enhanced Electron Transfer Photoanodes for Photovoltaic Applications

*Nian Li, Renjun Guo, Wei Chen, Volker Körstgens, Julian E. Heger, Suzhe Liang, Calvin J. Brett, Md Asjad Hossain, Jianshu Zheng, Peter S. Deimel, Ali Buyruk, Francesco Allegretti, Matthias Schwartzkopf, Jonathan G. C. Veinot, Guido Schmitz, Johannes V. Barth, Tayebeh Ameri, Stephan V. Roth, and Peter Müller-Buschbaum**

Based on a diblock-copolymer templated sol–gel synthesis, germanium nanocrystals (GeNCs) are introduced to tailor mesoporous titania (TiO_2) films for obtaining more efficient anodes for photovoltaic applications. After thermal annealing in air, the hybrid films with different GeNC content are investigated and compared with films undergoing an argon atmosphere annealing. The surface and inner morphologies of the TiO_2/GeO_x nanocomposite films are probed via scanning electron microscopy and grazing-incidence small-angle X-ray scattering. The crystal phase, chemical composition, and optical properties of the nanocomposite films are examined with transmission electron microscopy, X-ray photoelectron spectroscopy, and ultraviolet–visible spectroscopy. Special focus is set on the air-annealed nanocomposite films since they hold greater promise for photovoltaics. Specifically, the charge–carrier dynamics of these air-annealed nanocomposite films are studied, and it is found that, compared with pristine TiO_2 photoanodes, the GeNC addition enhances the electron transfer, yielding an increase in the short-circuit photocurrent density of exemplary perovskite solar cells and thus, an enhanced device efficiency as well as a significantly reduced hysteresis.

1. Introduction

Nanostructured titania (TiO_2) has established its prominence in many fields, such as photocatalysis,[1] lithium-ion batteries,[2] and photovoltaics.[3,4] This considerable research interest is closely related to its favorable chemical stability, wide bandgap, and large surface-to-volume ratio.[5,6] In particular, mesoporous titania films with interconnected network structures have been successfully implemented in photovoltaic devices such as hybrid solar cells (HSCs),[7] dye-sensitized solar cells (DSSCs),[8] quantum dot-sensitized solar cells (QDSSCs),[9] and perovskite solar cells (PSCs).[10] To date, the certified efficiency of DSSCs reached 12.3%,[11] while progress in PSC development has led to an impressive efficiency of >20%.[12] These advances strongly depended upon the development of superior sensitizers (dye molecules, quantum dots, perovskite

N. Li, R. Guo, Dr. W. Chen, Dr. V. Körstgens, J. E. Heger, S. Liang, Prof. P. Müller-Buschbaum
Lehrstuhl für Funktionelle Materialien
Physik-Department
Technische Universität München
James-Franck-Str. 1, 85748 Garching, Germany
E-mail: muellerb@ph.tum.de

Dr. C. J. Brett, Dr. M. Schwartzkopf, Prof. S. V. Roth
Deutsches Elektronen-Synchrotron DESY
Notkestr. 85, 22603 Hamburg, Germany

Dr. C. J. Brett
Department of Engineering Mechanics
KTH Royal Institute of Technology
Teknikringen 8, Stockholm 100 44, Sweden

The ORCID identification number(s) for the author(s) of this article can be found under https://doi.org/10.1002/adfm.202102105.

DOI: 10.1002/adfm.202102105

Dr. C. J. Brett
Wallenberg Wood Science Center
KTH Royal Institute of Technology
Teknikringen 56–58, Stockholm 100 44, Sweden

Dr. M. A. Hossain, Prof. J. G. C. Veinot
Department of Chemistry
University of Alberta
Edmonton, Alberta T6G 2E1, Canada

J. Zheng, Prof. G. Schmitz
Institute of Materials Science
University of Stuttgart
Heisenbergstr. 3, 70569 Stuttgart, Germany

Dr. P. S. Deimel, Dr. F. Allegretti, Prof. J. V. Barth
Physik-Department
Lehrstuhl für Molekulare Nanowissenschaften & Chemische Physik von Grenzflächen
Technische Universität München
James-Franck-Str. 1, 85748 Garching, Germany

A. Buyruk, Prof. T. Ameri
Chair of Physical Chemistry
Department of Chemistry
University of Munich (LMU)
Butenandtstr. 11, 81377 Munich, Germany

compounds) and/or hole-transport materials. In stark contrast, far fewer studies have focused on designing and tailoring the electron-transport layer (ETL) such as titania films, to achieve better photovoltaic device performance. Since the ETL is an inherent part of the functional stack forming the final device, its optimization also will be needed for further improvements in the device performance.

Tailoring the titania ETL has the potential to impact on a variety of photovoltaic technologies because it offers important advantages that include optimized energy levels, increased charge carrier concentration, and reduced interfacial recombination.[9,13,14] Among the available tailoring approaches, one that is particularly promising relies on the incorporation of (doping) metals, metal oxides, or semiconductors into the mesoporous titania. Germanium (Ge) and its oxides have attracted enormous attention in this regard, because of several beneficial properties: (1) Ge shows a very high electron mobility, which is higher than that of silicon.[15] (2) The optical transparency in visible and near-ultraviolet regions and the wide bandgap enable GeO_2 to be utilized like other transparent conducting oxides such as tin oxide (SnO_2) and TiO_2.[16] (3) In the absence of water, Ge/GeO_x materials exhibit a small hysteresis behavior.[15] These advantages make Ge and its oxides interesting for the optoelectronic industry,[17,18] and thus, it is hypothesized that the introduction of them could improve the electronic (and optical) characteristics of TiO_2 for solar cell applications. Previous studies showed that adding germanium oxide to TiO_2 anodes provided an alternative approach to improve the DSSC efficiency.[19,20] Duan et al. designed TiO_2/GeO_2 nanocrystallite anodes to enhance the interference light intensity, consequently increasing the electron density.[19] Simultaneously, attention was paid to TiO_2-Ge composites for their potential application in photovoltaics.[21–23] The photoconductivity of TiO_2-Ge films suggested that the nanocomposite can be an ideal photovoltaic semiconductor.[21] Ahmad et al. also reported that the nanocomposite TiO_2 with 2 wt% Ge nanoparticles showed improved electron transfer ability compared to pristine TiO_2 nanoparticles.[22]

To date, so-called diblock-copolymer (DBC)-assisted sol-gel synthesis has proven to be a favorable route to establish titania nanostructures in a controlled fashion.[24,25] The general sol-gel approach provides a facile solution deposition route that is readily compatible with a variety of film deposition processes ranging from laboratory-scale coating like spin coating[26] to industrial-scale coating like spray coating[27] and slot-die printing.[25] Sol–gel methods also facilitate the dopant incorporation and the resulting doped-films can possess uniform morphology with continuous and pinhole-free structures.[28] With the utilization of a DBC, which acts as a structure-directing template, a large variety of nanostructures can be achieved by self-assembly.[29] In our study, due to the surface functionalization, the germanium nanocrystals (GeNCs) maintain their solubility in solvents and have a preferential selectivity to a specified block of a DBC.[30,31] In addition, due to effects like steric hindrance, the possibility of forming big GeNC agglomerates can be mitigated by the DBC matrix.[31] These factors contribute to the exquisite tailoring of the mesoporous TiO_2 nanostructures by introducing GeNCs in combination with the metal oxide precursor.

In the present work, we report a new approach that combines dodecyl functionalized GeNCs of 7–9 nm average sizes with the sol–gel chemistry and affords ordered mesoporous TiO_2/GeO_x films. By doing so, we have succeeded in improving the electronic characteristics, such as the electron transfer mobility and hysteresis behavior of PSCs, via introducing GeNCs in TiO_2 photoanodes.[15,32]

GeNCs are added to the titania sol–gel reaction mixture in a series of pre-defined GeNCs:TiO_2 weight ratios. The sol–gel reaction mixture consists of an amphiphilic DBC template polystyrene-*block*-polyethylene oxide (PS-*b*-PEO) and a titania precursor titanium(IV)isopropoxide (TTIP). Thermal annealing in air removes the PS-*b*-PEO template and the aliphatic surface functionalities on the GeNC surfaces; this process yields mesoporous TiO_2/GeO_x nanostructures. For comparison and also to obtain a purer Ge phase, argon atmosphere-annealed nanocomposite films are also prepared. The resulting surface and inner morphologies are investigated via scanning electron microscopy (SEM) and grazing incidence small-angle X-ray scattering (GISAXS), respectively. The crystalline properties and elemental composition of the nanocomposite films are probed by X-ray diffraction (XRD) and transmission electron microscopy (TEM), and X-ray photoelectron spectroscopy (XPS), respectively. The optical properties are observed via ultraviolet–visible spectroscopy (UV–vis). Irrespective of the GeNC addition, the air-annealed nanocomposite films possess ordered mesoporous morphologies, high crystallinity, and good transparency, which appear highly promising for solar cell applications. By comparison, the Ge richer phase obtained from films annealed in argon atmosphere are less promising because they show lower transmittance. In this context, we focus on the air-annealed nanocomposite films concerning use in photovoltaics and explore their application as photoanodes in PSCs. To better understand the photovoltaic characteristics of the air-annealed nanocomposite films, we choose to investigate their charge carrier dynamics and find that introducing GeNCs can boost the electron transfer from the perovskite layer to the ETL, which contributes to an increased short-circuit photocurrent density (J_{sc}), thus achieving an enhanced power conversion efficiency (PCE). Simultaneously, the addition of GeNCs can strongly suppress the hysteresis of the PSCs. This knowledge is of great significance for tailoring the mesoporous TiO_2 films for efficient photoanodes and is expected to be useful in other solar cell systems as well, such as, DSSCs.

Prof. S. V. Roth
Department of Fibre and Polymer Technology
KTH Royal Institute of Technology
Teknikringen 56–58, Stockholm 100 44, Sweden
Prof. P. Müller-Buschbaum
Heinz Maier-Leibnitz Zentrum (MLZ)
Technische Universität München
Lichtenbergstr. 1, 85748 Garching, Germany

2. Results and Discussion

2.1. Film Morphology

To investigate the influence of pre-synthesized GeNCs on the morphology of mesoporous TiO_2 films, we prepare five

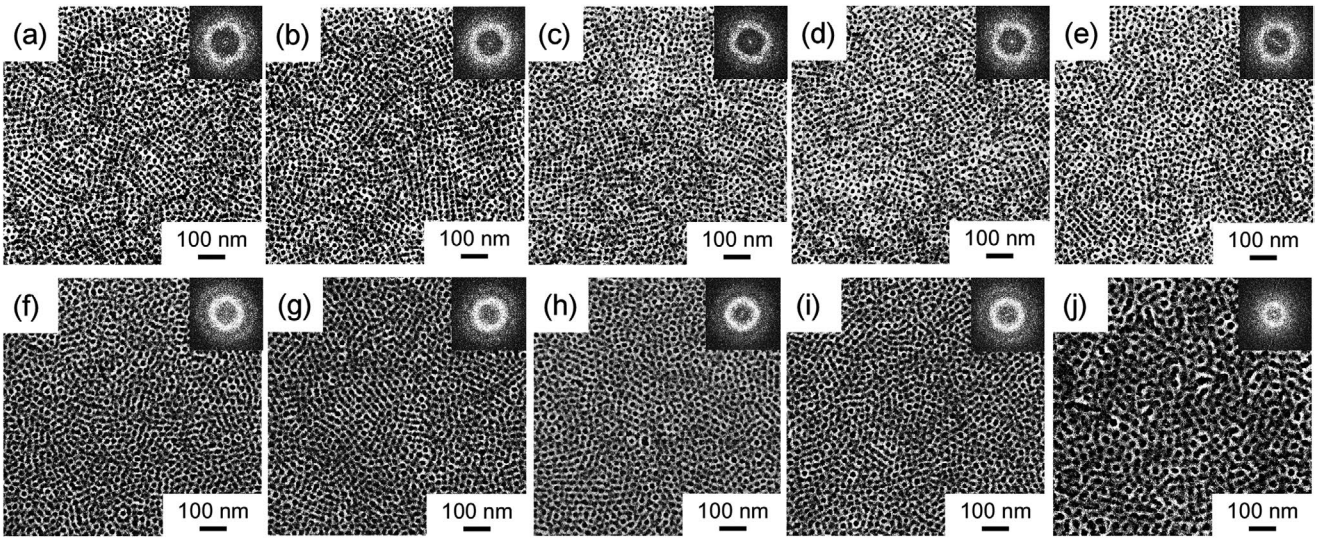

Figure 1. Top-view secondary electron SEM images of the TiO_2/GeNC films after thermal annealing at 500 °C in air: a) 0 wt%, b) 0.5 wt%, c) 1.0 wt%, d) 2.5 wt%, and e) 5.0 wt% GeNCs, or in argon atmosphere: f) 0 wt%, g) 0.5 wt%, h) 1.0 wt%, i) 2.5 wt%, and j) 5.0 wt% GeNCs. Insets show corresponding 2D-FFT patterns.

films containing pre-defined weight contents of GeNCs (wt% GeNCs in TiO_2 of 0, 0.5, 1.0, 2.5, and 5.0; samples are denoted as 0 wt% GeNCs, 0.5 wt% GeNCs, 1.0 wt% GeNCs, 2.5 wt% GeNCs, and 5.0 wt% GeNCs, respectively) via a DBC-assisted sol–gel method. After spin coating, the hybrid TiO_2/GeNC/PS-*b*-PEO films are thermally annealed at 500 °C in air or argon atmosphere for 2 h. The Fourier transform infrared (FTIR) data (Figure S1, Supporting Information) indicates that the polymer template PS-*b*-PEO is completely removed through the thermal annealing treatment.

Figure 1 shows representative secondary electron SEM images of the TiO_2/GeNC film surfaces after thermal annealing in air or argon atmosphere. All air-annealed TiO_2/GeNC films display similar well-defined sponge-like nanostructures (i.e., a mesoporous structure with an interconnected network, Figure 1a–e), which indicates that the addition of GeNCs does not influence the overall film surface morphologies. Close inspection reveals hexagonal and square mesopore packings (Figure S2, Supporting Information) on the film surfaces that are similar to what has been previously reported for the surface structure of TiO_2/PS-*b*-PEO hybrid films.[33] To further evaluate the degree of structural order in the present films, 2D fast Fourier transform (2D-FFT) patterns are calculated from the respective SEM images and shown as insets in Figure 1a–e. A first-order ring is seen in the 2D-FFT of the 0 wt% GeNCs film consistent with the presence of a well-defined nearest-neighbor ordering of the nanostructures. Importantly, the degree of order is not deteriorated by adding the GeNCs. The related power spectral density (PSD) functions (Figure S3a, Supporting Information) display a similar q value for the position of the correlation peak for all TiO_2/GeNC films (gray dashed line). It suggests that irrespective of the amount of GeNCs, the average center-to-center distances of the nanostructures have a value of 23.0 ± 0.5 nm in the case of the TiO_2/GeNC films annealed in air. In contrast to the air-annealed films, the morphologies and 2D-FFT patterns of the argon atmosphere-annealed films (see Figure 1f–i) change at 5.0 wt% GeNCs. Only at lower GeNC concentrations (0 to 2.5 wt%), the morphologies and characteristic center-to-center distances of the nanostructures remain unchanged. At 5.0 wt% GeNCs, the surface morphology is changed (Figure 1j) and shows a reduced degree of order as seen from the 2D-FFT pattern and PSD functions (Figure S3b, Supporting Information). Thus, the higher GeNC loading starts to perturb the DBC-templating and thereby deteriorates the structure regularity when films are processed using argon atmosphere annealing.[34]

All samples possess mesoporous structures with an interconnected network suggesting the annealing atmospheres play a minor role in the formation of a porous sponge-like morphology. In addition, the TiO_2/GeNC films annealed in air have a smaller average nanoparticle size than that in argon atmosphere, which agrees well with the observation reported elsewhere.[35]

In addition to the surface morphologies, the buried structures of the present films are of importance because they directly influence charge carrier transport and the final device performance.[36] To gain additional insight into the nature of the internal morphologies of the films in terms of characteristic structures like center-to-center distances and radii of the TiO_2/GeO_x domains, GISAXS measurements are performed.

From the 2D GISAXS data of the TiO_2/GeNC films after thermal annealing in air (**Figure 2**), all samples show a prominent Bragg peak (Figure 2a; magenta arrow) in the GISAXS data together with its second-order and weak third-order peaks (Figure 2a; green and orange arrows, respectively). The occurrence of higher-order peaks reveals the presence of well-ordered nanostructures within the films. Simultaneously, the observation of a third-order peak, even at higher GeNC contents, suggests that the addition of GeNCs is not accompanied by a loss of internal structural order. Moreover, two sharp rod-like Bragg peaks (Figure 2d; red arrows) located at $q_y \approx 0.17$ and 0.28 nm^{-1} are observed that originate from the scattering signal of the

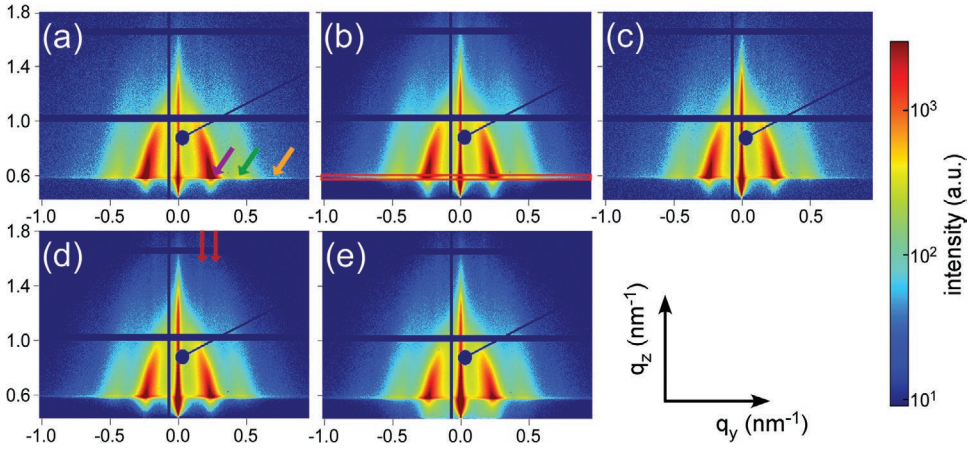

Figure 2. 2D GISAXS data of the TiO_2/GeNC films after thermal annealing at 500 °C in air: a) 0 wt%, b) 0.5 wt%, c) 1.0 wt%, d) 2.5 wt%, and e) 5.0 wt% GeNCs. Colored arrows denote Bragg peaks caused by the highly ordered inner structures: first-order (magenta), second-order (green), and third-order (orange). The two red arrows highlight a rod-like Bragg peak and its second-order peak, originating from the surface structures.

surface ordered nanostructures.[33] The ratio of the q_y values is 1.65 (close to $\sqrt{3}/1$), which suggests the TiO_2/GeO_x nanoparticles are predominantly hexagonally packed on the film surfaces, reported elsewhere.[33]

To get further insight into the influence of GeNC addition on the internal nanostructure of the presented films, horizontal line cuts of the 2D GISAXS data are made at the Yoneda peak position of TiO_2/GeO_x (Figure 2b; red box). To extract the lateral structure characteristics, line cuts are modeled within the framework of the distorted wave Born approximation (DWBA) together with the effective interface approximation (EIA) and the local monodisperse approximation (LMA).[37–40] A detailed description of this GISAXS modeling can be found elsewhere.[41] Cylinder form factors have been successfully used to model the nanostructures in mesoporous films in the literature,[25,41,42] and thus are applied in the present data analysis. The horizontal line cuts and modeling results for the air-annealed films are shown in **Figure 3**a. The strong Bragg peak (magenta arrow) and its two weaker higher-order peaks (green and orange arrows) are evident in all profiles. These features emphasize long-range lateral correlations in the highly-ordered inner nanostructures. Two characteristic center-to-center distances (structure factors) and radii (form factors) are extracted from the GISAXS modeling and plotted as a function of GeNC content in Figure 3b,c. The small-sized structures (i.e., Figure 3; olive crosses) exhibit similar nanoparticle radii and center-to-center distances (within error bars) in all films, irrespective of the GeNC content. For example, the pristine mesoporous TiO_2 film has nanoparticle radii and corresponding center-to-center distances of 5.3 ± 0.1 nm and 25.8 ± 0.1 nm, respectively. Compared with the large-sized structures (i.e., Figure 3; red squares), the size distribution of the center-to-center distances is narrower for the small-sized structures (Figure S6, Supporting Information). Thus, the small-sized structures are more ordered compared to their larger counterparts. However, their size distribution broadens with increasing GeNC contents (as seen in Figure S6a, Supporting Information, olive crosses). From this, we conclude that, not surprisingly, introducing GeNCs worsens the degree of order. A different tendency is observed for the large-sized structures. The corresponding radii (within error bars) again do not change with GeNC addition, but the center-to-center distances (within error bars) increase with increasing GeNC contents. The radii of the large-sized structures for the 0 wt%, 0.5 wt%, 1.0 wt%, 2.5 wt%, and 5.0 wt% GeNCs are 9.7 ± 0.2, 9.8 ± 0.2, 9.7 ± 0.2, 9.6 ± 0.2, and 9.8 ± 0.1 nm, and the corresponding center-to-center distances are 23 ± 0.3, 24.6 ± 0.7, 25 ± 0.7, 26 ± 0.5, and 26.7 ± 0.5 nm. Since the hydrophobic dodecyl chains cause the GeNCs to be preferentially incorporated inside the PS domains of the templating polymer, adding GeNCs expands the PS domains resulting in larger center-to-center distances. We also note a broader size distribution in the center-to-center distances with increasing GeNC contents (Figure S6a, Supporting Information; red squares). This increase in the interdomain distance and distribution width is similar to the DBC templating of magnetic nanoparticles reported previously.[34,43] Based on the model used above, the average pore size is calculated with Equation (S1), Supporting Information (details can be found here).[25] For air-annealed and argon atmosphere-annealed films, we find that the pore sizes originating from small-sized structures are independent of the GeNC content (Figure S7a,b, Supporting Information; olive crosses). In contrast, the average pore sizes of the large-sized structures show a slight dependence on the GeNC content with the largest value reached in the 2.5 wt% GeNCs films (Figure S7, Supporting Information).

Applying the same analysis to the data of the argon atmosphere-annealed nanocomposite films, horizontal line cuts are analyzed (Figure S5a, Supporting Information) and the corresponding extracted center-to-center distances and radii are determined (Figure S5b,c, Supporting Information). In general, the small-sized and large-sized nanostructures show the same general trends as observed for air-annealing. However, when comparing directly, the argon atmosphere-annealed films exhibit larger nanoparticle radii (see Supporting Information). Spectroscopic ellipsometry (SE) data (Figure S8, Supporting Information) show that annealing in argon atmosphere yields a slightly larger porosity of the titania film than annealing in air, which is in agreement with the larger average mesopore sizes

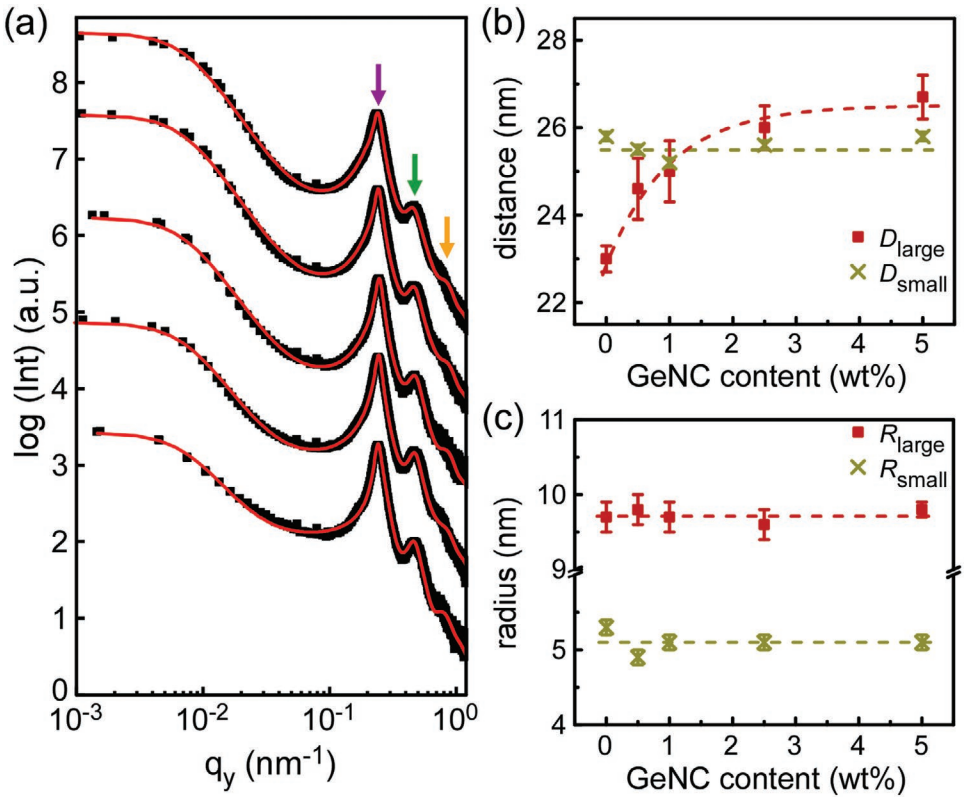

Figure 3. a) Horizontal line cuts of the 2D GISAXS data of the TiO_2/GeNC films after thermal annealing at 500 °C in air: 0 wt%, 0.5 wt%, 1.0 wt%, 2.5 wt%, and 5.0 wt% GeNCs from bottom to top. Colored arrows highlight peaks arising from the highly ordered inner structures: first-order (magenta), second-order (green), and third-order (orange). Extracted characteristic length scales: b) Center-to-center distances and c) nanoparticle radii as a function of GeNC content. Olive crosses indicate the small-sized structures, and red squares the large-sized structures. The dashed lines are provided as a guide to the eye.

of the argon atmosphere-annealed film (Figure S7, Supporting Information). Moreover, this finding also agrees well with the observation reported recently.[42]

To illustrate the influence of GeNC addition on the titania morphology, an illustration of the evolution of the titania-DBC films with incorporated GeNCs is presented in **Figure 4**. With a so-called good–bad solvent pair, the PS-*b*-PEO diblock copolymer undergoes a micro-phase separation and self-assembles into spherical micelles.[44] The titania precursor TTIP prefers being coordinated with the PEO domains through hydrogen bonds, while GeNCs favor the PS domains due to the dodecyl surface functionalization (Figure 4a). At low concentrations

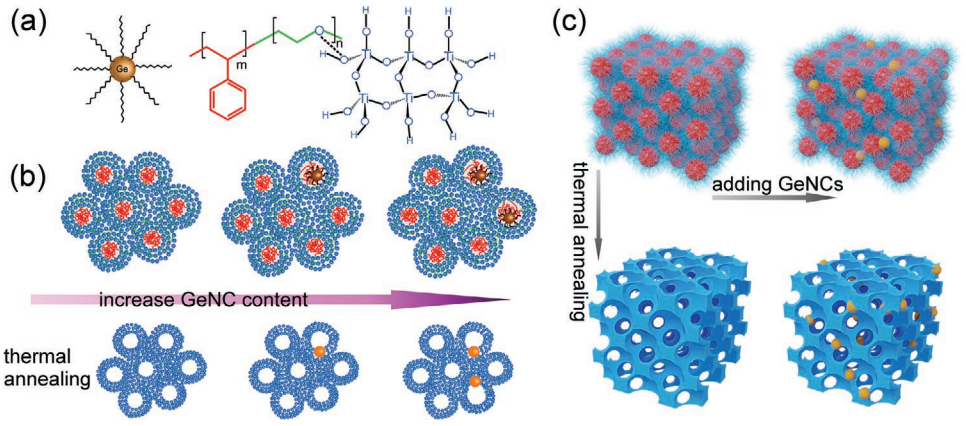

Figure 4. Illustrations of a) dodecyl-capped GeNCs, PS-*b*-PEO diblock copolymer, titania precursor (blue), and hydrogen bonding interaction between the titania precursor and the PEO block, b) Nanostructure evolution of the TiO_2/PS-*b*-PEO films with GeNC concentrations before and after thermal annealing. c) A 3D representation of the TiO_2/PS-*b*-PEO film with and without GeNCs after thermal annealing. In both (b,c), hydrolyzed titania nanoparticles are indicated in blue, the PS domains indicated in red, and GeNCs indicated in brown. After thermal annealing, the polymer is removed in (b,c) and mesoporous crystallized TiO_2 (blue) with or without GeO_x nanoparticles (orange) form.

(i.e., ≤5 wt%), GeNCs are expected to reside within the PS domains (Figure 4b) and cause the PS domains to expand. This expansion results in an increased center-to-center distance. During thermal annealing in air (or argon atmosphere), TiO_2 crystallizes, GeO_x forms (details are explained below), together with the removal of the organic chains. Due to the applied high-temperature heating, the neighboring nanoparticles fuse into larger ones.[45,46] The identified size of the GeO_x nanoparticles from high-resolution TEM (HRTEM) of ≈10 nm (Figure S9a,b, Supporting Information) agrees well with the initial GeNC sizes of 7–9 nm[30] and matches well with twice the small-sized radii found in GISAXS (e.g., Figure 3c). In addition, it is reasonable to assume that the GeO_x nanoparticles will also fuse to the neighboring TiO_2, and thus develop into larger sizes (more than 10 nm), as referred to the large-sized structures in the GISAXS analysis. Therefore, we observe that the center-to-center distances of the large-sized structures increase, while the majority of the inner morphologies, namely the small-sized structures, remain unchanged due to the absence of GeNC incorporation (Figure 4c).

2.2. Crystallinity

XRD and TEM are used to identify the crystal phase and crystallinity of the nanocomposite films, since these key parameters play a critical role in the photogenerated charge carrier transport. As a reference, the diffraction peaks from anatase TiO_2, GeO_2, and a diamond cubic Ge phase are indicated at the bottom.[49,50,52] All diffraction patterns are consistent with the anatase titania phase (PCPDS #21-1272) with its pronounced (101) and (004) diffraction peaks (**Figure 5**g,h).[47] The crystallite sizes are estimated from the TiO_2 (101) peak via the Scherrer equation, analyzing the XRD line broadening. The crystallite sizes for the 0 wt%, 0.5 wt%, 1.0 wt%, 2.5 wt%, and 5.0 wt% GeNCs (annealed in air) almost remain constant within the error bars (7.4 ± 0.3, 7.5 ± 0.3, 7.1 ± 0.3, 7.4 ± 0.3, and 7.3 ± 0.3 nm, respectively). A similar tendency is seen in the GISAXS study of the characteristic nanoparticle radii of the air-annealed films. Small differences in the absolute numbers show that not the entire nanoparticles are crystalline. Because of the very low GeNC content, it is difficult to analyze the crystal structure of the GeNCs in the composite films after thermal annealing. Thus, the nanocomposite films

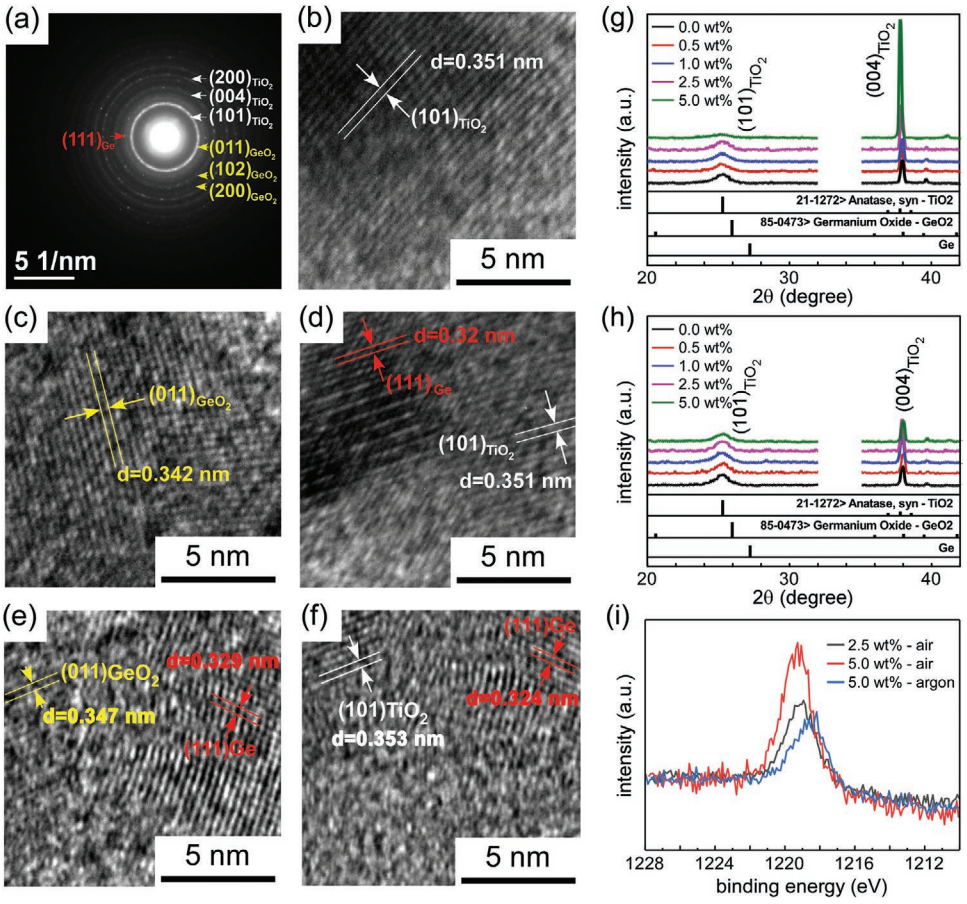

Figure 5. a) SAED pattern and b–d) HRTEM images of the TiO_2/GeNC film with 5.0 wt% GeNCs after thermal annealing in air, e,f) HRTEM images of a representative TiO_2/GeNC film containing 5.0 wt% GeNCs after thermal annealing in argon atmosphere. XRD patterns of the TiO_2/GeNC films with different GeNC contents as indicated after thermal annealing in g) air and h) argon atmosphere. The curves are shifted along the y axis for clarity of the presentation and the angular range from 32° to 35° is blocked to avoid the strong Bragg peak of the Si substrate. i) Ge $2p_{3/2}$ XPS spectra of representative TiO_2/GeNC films after thermal annealing in air: 2.5 wt% (black), 5.0 wt% (red) GeNCs, and in an argon atmosphere: 5.0 wt% (blue) GeNCs.

with the highest GeNC content (i.e., 5.0 wt%) are further evaluated using TEM. The selected area electron diffraction (SAED) data of the film after annealing in air (Figure 5a) presents a series of diffraction rings corresponding to crystallites of the anatase TiO_2 phase and hexagonal GeO_2 (JCPDS #85-0473).[48] In addition, a diamond cubic Ge phase is detected,[49] which is in agreement with the findings from Ge-based thin films prepared via a sol-gel synthesis before.[50] From the center to the exterior region, the first three rings of the anatase TiO_2 phase correspond to reflections from the (101), (004), and (200) planes, and the first three rings of the GeO_2 phase correspond to reflections from the (011), (102), and (200) planes.[25,48] In the case of the Ge phase, only the (111) reflection is observed. The related HRTEM images (Figure 5b–d) display well-resolved lattice spacings of 0.351, 0.342, and 0.320 nm, being consistent with the lattice spacing of TiO_2 (101),[25] as well as GeO_2 (011),[48] and Ge (111) planes,[49,50] respectively. The same results are obtained in the HRTEM images of the argon atmosphere-annealed 5.0 wt% GeNCs film (Figure 5e,f). Evidence for GeO_2 remains, even though its formation is hindered due to the oxygen-poor environment. An explanation for this observation is that the titania precursor and the PEO blocks could deliver oxygen to the system.[50] In addition, one must also consider that the GeNCs themselves could contribute some oxide impurities.[30,49] The absence of GeO in the TEM measurements for both samples can be explained by the poor crystallinity of GeO.[51]

2.3. Chemical Composition

To get insight into the elemental and chemical composition of the presented nanocomposite films, we use XPS. This technique is intrinsically surface-sensitive and thus delivers information on the outermost layers of the films (typically within 10 nm below the surface). Figure 5i shows the normalized Ge $2p_{3/2}$ spectra of the TiO_2/GeNC films after annealing under the indicated conditions. (Details of the XPS measurements as well as data calibration and fits are found in the Supporting Information). For the TiO_2/GeNC films annealed in air (2.5 and 5.0 wt% GeNCs), the Ge $2p_{3/2}$ core-level emission is shifted to higher binding energies compared to the spectral features of the 5.0 wt% GeNCs films annealed in argon atmosphere. This observation is consistent with more elemental (or incompletely oxidized) Ge being present in the argon atmosphere-annealed films. All XPS spectra are fitted with Gaussian functions after subtraction of a Shirley-type background (Figure S10, Supporting Information). We find that three spectral components are necessary: one is located at a binding energy of ≈1217.3 eV and can be associated with elemental Ge, while the other two at higher binding energies of ≈1218.9 and ≈1220.0 eV are attributed to GeO and GeO_2, respectively.[53,54] Thus, Ge, GeO_2, as well as GeO are present in the nanocomposite films. The presence of GeO can be rationalized by considering that the reversible reaction ($2GeO \leftrightarrow GeO_2 + Ge$) might occur during thermal annealing at 500 °C,[55,56] in addition to the oxygen deficiency of the argon atmosphere annealing environment. The binding energy positions of individual components are the same in both, the air- and argon atmosphere-annealed films. In the former, the total spectral intensity for the 2.5 wt% GeNCs film is approximately half of that in the 5.0 wt% GeNCs. This intensity ratio is reasonably expected, given the GeNC concentration ratio. The 5.0 wt% GeNCs film annealed in argon atmosphere shows a lower spectra intensity as compared to the air-annealed analogue (Figure 5i), which might arise from its unique surface morphology as seen in Figure 1j.[57]

2.4. Optical Properties

To examine the optical transmittance of the present nanocomposite films in dependence of the GeNC content, the films are deposited on glass substrates. The sharp decrease observed in all transmittance spectra (**Figure 6**) in the 280–350 nm range is related to the optical absorption of the materials. Irrespective of the GeNC content, all air-annealed films exhibit near 100% transparency in the visible spectra region (Figure 6a). In contrast, the transmittance of films annealed in an argon atmosphere is reduced, although it remains above 90% in all cases (Figure 6b). A reasonable explanation for this lower transmittance is films annealed in argon atmosphere exhibit larger average grain sizes that are known to lead to decreased transmittance.[58] The optical band gap of the synthesized nanocomposite films are estimated using the Tauc equation (Figure S11, Supporting Information). The determined band gaps for air- and argon atmosphere- annealed films (see Supporting

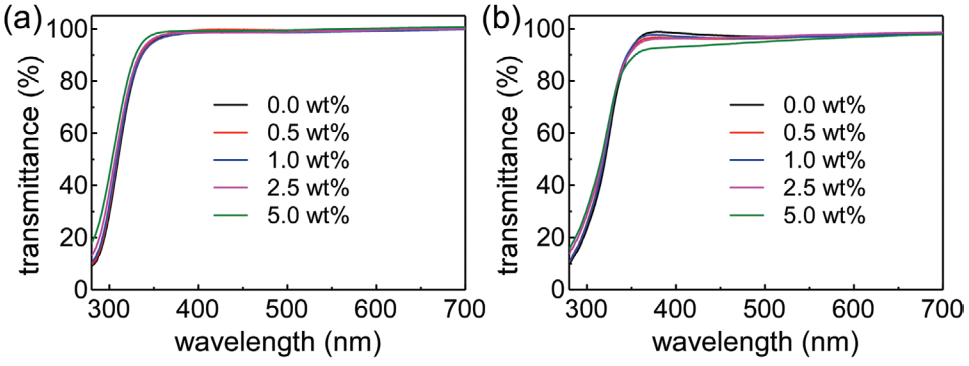

Figure 6. Transmittance spectra of the TiO_2/GeNC films containing indicated GeNC contents after thermal annealing in a) air and b) argon atmosphere. The glass substrate is used as a reference sample for the transmission measurement.

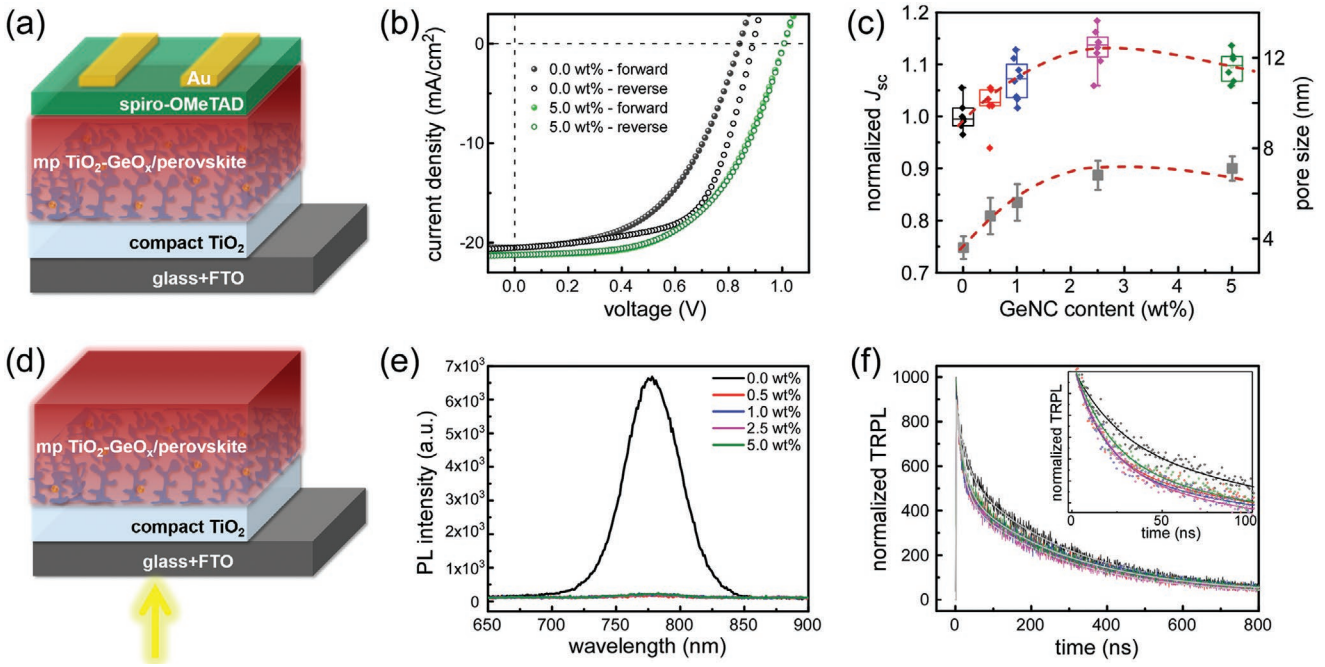

Figure 7. Pictorial representation of a) full PSC device using the investigated ETL layers and d) respective partial functional stack for steady-state PL and TRPL measurements. b) Hysteresis behavior in the *J–V* measurements of PSCs based on the 0.0 wt% (black) and 5.0 wt% GeNCs (green) films. c) Normalized J_{sc} values and pore sizes of the large-sized structures (gray squares) as a function of GeNC content. The dashed lines are guides to the eye. e) Steady-state PL and f) TRPL spectra (symbols) with corresponding fits (solid lines) of the TiO_2/GeNC films for different GeNC content after thermal annealing in air. The inset panel in (f) focuses on the spectra within 0–100 ns. Different colors indicate different ETLs: 0.0 wt% GeNCs (black), 0.5 wt% GeNCs (red), 1.0 wt% GeNCs (blue), 2.5 wt% GeNCs (magenta), and 5.0 wt% GeNCs (green).

Information for more details) are similar to the band gap of their respective pristine mesoporous anatase titania with nanostructures, implying that the introduction of GeNCs in the presented concentrations does not significantly affect the band gap.

2.5. Charge Carrier Dynamics and PSC Performance

We further investigate the charge carrier dynamics of the air-annealed films and fabricate perovskite solar cells based on them (**Figure 7**a). The PSC fabrication follows a standard methodology detailed in the Supporting Information that focuses on realizing identical devices,[59] which differ only in the ETL (air-annealed TiO_2–GeNC films).

To study charge carrier dynamics in air-annealed nanocomposite films, the perovskite is coated on the ETL of choice. A compact TiO_2 layer coated on FTO/glass is used as the substrate to maintain the same functional stack as in the common PSC device architecture (Figure 7d). Compared with the pristine TiO_2 film, marked photoluminescence (PL) quenching is observed in the FTO/compact TiO_2/mesoporous TiO_2–GeNC/perovskite systems (Figure 7e), indicating that the electron mobility of the ETLs is enhanced by the introduction of GeNCs. Accordingly, we use these ETLs in the PSC fabrication. The PSC devices using a pristine TiO_2 anode (without GeNCs) show the well-known hysteresis behavior in the *J–V*-characteristics (Figure 7b), in which the reverse scan exhibits a higher performance than that of the forward scan.[60] In contrast, with the addition of 5.0 wt% GeNCs to the composite film used as the ETL, the hysteresis phenomena are strongly suppressed (Figure 7b). Moreover, the addition of GeNCs enhances the J_{sc} (Figure S12b, Supporting Information), thereby improving the PCE (Figure S12a, Supporting Information) of the devices. The similar open-circuit voltages (V_{oc}, Figure S12c, Supporting Information) of the PSCs demonstrate that the energy levels between the ETLs and the perovskite layer remain unchanged,[61] because the bandgap of the mesoporous titania films used as the ETLs is not tuned by the GeNCs addition (Figure S11, Supporting Information). The highest J_{sc} and PCE values are observed in the case of the 2.5 wt% GeNCs films, which might be attributed to the presence of the largest pores in these films (as exemplarily highlighted in Figure 7c). Larger pores can allow for a better infiltration of the perovskite, and a more efficient contact between the mesoporous ETL and perovskite.[62] These improvements can enhance the electron injection from the perovskite into the ETL.[62]

To understand the charge carrier separation at the ETL/perovskite interface, we perform time-resolved PL (TRPL) measurements on perovskite deposited on the different ETLs. The TRPL curves are fitted with a two-phase exponential decay function,[63] and the corresponding fits are plotted as solid lines in Figure 7f. The extracted lifetimes and amplitude fractions are summarized in Table S1, Supporting Information. Compared with the pristine film, the charge carrier lifetime is decreased for the composite films. Moreover, 1.0 wt% and 2.5 wt% GeNCs samples exhibit clear larger proportions of the fast component, which could indicate a better energy transfer configuration.[64]

We deduce that the charge carriers can be efficiently and rapidly separated from the perovskite layer to the ETL due to the GeNC addition.[65] This enhanced charge carrier extraction can be attributed to the intrinsic property of a high electron mobility of the ETLs established by introducing GeNCs.[32] This advantage leads to an overall improvement in the photovoltaic performance by increasing the J_{sc} and PCE values. Note also that the shortest average charge carrier lifetime is present in the 2.5 wt% GeNCs sample, which agrees well with the above result of the best performing PSC at this composition.

3. Conclusion

In this work, we demonstrate that ordered mesoporous TiO_2 films can be finely tailored through the inclusion of pre-synthesized GeNCs into a diblock-copolymer templating sol–gel synthesis protocol, displaying a successful strategy to obtain efficient photoanodes upon high-temperature annealing. The effect of GeNC addition on the mesoporous TiO_2 film is investigated by means of SEM, GISAXS, XRD, TEM, XPS, and UV–vis spectroscopy. Our measurements reveal that upon GeNC addition, the composite TiO_2/GeO_x films maintain ordered mesoporous morphologies, high crystallinity, and good transparency in the visible range. Moreover, the inner morphology consists of small-sized structures, which have similar center-to-center distances and radii irrespective of the GeNC addition. The large-sized structures are also present, which display nearly constant radii and increasing center-to-center distances with the increasing amount of GeNCs. Among the investigated samples, the largest pore sizes are found in the 2.5 wt% GeNCs sample. The air-annealed nanocomposite films are used as ETLs in PSCs. Compared to pristine TiO_2 photoanodes, the GeNC addition enhances the electron transfer, thereby yielding an overall improvement in the J_{sc} and PCE values. Moreover, it strongly suppresses the well-known hysteresis behavior in the PSCs. Best performing devices are observed at 2.5 wt% GeNCs addition.

While the work presented here is far from an optimization of the device parameters, it demonstrates the clear improvements achieved with controllable nanostructures in the ETLs. The simple synthesis protocol makes the composite TiO_2/GeO_x films highly interesting as anode candidates in photovoltaics. Moreover, the method of combining GeNCs with the sol–gel synthesis of mesoporous metal oxide films can be transferred to other metal oxides such as zinc oxide (ZnO) or SnO_2, thus providing a viable route for fabricating ordered mesoporous nanocomposite films with a variety of materials. The comparison between air and argon atmosphere annealing outlines a way for producing TiO_2/GeO_x nanocomposite semiconductors to meet various needs for applications also beyond PSCs.

4. Experimental Section

Preparation of Porous Nanocomposite Films: Titania films with five pre-defined concentrations of pre-synthesized germanium nanocrystals (GeNCs) were fabricated. For the TiO_2 sol–gel synthesis, the diblock copolymer polystyrene-*block*-polyethylene oxide (PS-*b*-PEO) played the role as a structure-directing template and titanium(IV)isopropoxide (TTIP) as a titania precursor. The toluene (T) and 1-butanol (B) mixed solvent and hydrochloric acid (HCl) served as a so-called "good–bad" solvent pair. The details about chemicals can be found in the Supporting Information. First, 100 mg PS-*b*-PEO was dissolved in a TB mixed solvent (3607 µL, 72.8 wt% toluene and 27.2 wt% 1-butanol forming a binary azeotrope[44]). After 30 min, a polytetrafluoroethylene (PTFE) filter with a pore diameter of 0.2 µm was used to filter the completely dissolved polymer solution. Subsequently, 382.4 µL TTIP was added into the polymer solution after diluting by 500 µL TB solvent. Similarly, 101.4 µL HCl was diluted with 500 µL TB solvent and then cautiously added dropwise under vigorous stirring. Finally, the titania sol–gel solution was stirred for about 30 min at room temperature.

GeNCs with dodecyl chains and average sizes of 7–9 nm were pre-synthesized as described elsewhere.[30] The dodecyl functionalization enabled GeNCs to be stored as a toluene suspension for further utilization.[30] Five different types of solutions with the weight ratios of GeNCs to TiO_2 of 0, 0.5, 1.0, 2.5, and 5.0 wt% were prepared as follows. The sol–gel solution was divided into five portions, each of 700 µL. After ultrasonic dispersion for ≈10 min, GeNCs (5 mg mL^{-1}) were added into these five specified portions with the volumes of 0, 14.2, 28.4, 71.0, and 142.0 µL, separately. After stirring for 30 min, spin coating was performed on silicon (Si) and glass substrates (2000 rpm for 60 s). Oxygen plasma cleaning (10 min, 200 W) of the substrates was used to improve the film homogeneity. The obtained hybrid TiO_2/GeNC films with the polymer template were annealed in air or argon atmosphere at 500 °C for 2 h with a heating rate of 5 °C min^{-1} to completely remove the polymer template.

Film Characterization: The surface morphology was measured by a field-emission SEM (Zeiss NVision 40). GISAXS measurements were carried out at the P03/MiNaXS beamline of the PETRA III storage ring at DESY (Hamburg, Germany).[66] The X-ray wavelength was 1.05 Å (X-ray energy of 11.7 keV) and the sample-to-detector distance (Dectris Pilatus 1M) was 3426 mm. The incident angle was selected at 0.41°, which was above the critical angles of Si/SiO_x (0.15–0.16°), bulk TiO_2 (0.20°), bulk Ge (0.21°), and bulk GeO_2 (0.19°), respectively, according to scattering length density calculations. Therefore, the X-rays could penetrate the entire films to probe inner structures. The crystal phase of the TiO_2/GeNC films was monitored by an X-ray diffractometer with Cu Kα radiation (Bruker D8 ADVANCE) and transmission electron microscopy (PHILIPS CM200-FEG). The X-ray photoelectron spectroscopy (XPS) measurements were performed in a custom-built ultra-high vacuum (UHV) chamber, which included a conventional twin-anode X-ray source (PSP Vacuum Technology) and a hemispherical electron energy analyzer (ES200 spectrometer, AEI Scientific Apparatus Ltd). For recording the Ge $2p_{3/2}$ core-level spectra, non-monochromatized Al Kα radiation (1486.6 eV) was used. The optical transmittance spectra of the nanocomposite films on the glass substrate were measured with a Lambda 35 UV–vis spectrometer (PerkinElmer) with a wavelength range from 280 to 700 nm. For the air-annealed films, steady-state photoluminescence (PL) and time-resolved photoluminescence (TRPL) measurements were carried out on a Picoquant Fluotime 300 spectrofluorometer with an excitation wavelength of 370 nm. The details on the characterization techniques and solar cell fabrication are provided in the Supporting Information.

Supporting Information

Supporting Information is available from the Wiley Online Library or from the author.

Acknowledgements

This work was supported by funding from the Deutsche Forschungsgemeinschaft (DFG, German Research Foundation) under Germany´s Excellence Strategy – EXC 2089/1 – 390776260 (e-conversion), TUM.solar in the context of the Bavarian Collaborative

Research Project Solar Technologies Go Hybrid (SolTech), the Center for NanoScience (CeNS), and the International Research Training Group 2022 Alberta/Technical University of Munich International Graduate School for Environmentally Responsible Functional Hybrid Materials (ATUMS). A. H. and J. G.C.V. acknowledge the continued generous funding from the Natural Science and Engineering Research Council (NSERC Discovery Grant program) as well as the Canadian arm of the ATUMS training program that is supported by NSERC CREATE, Alberta Innovates Strategic Projects, Future Energy System (FES) which is supported by the Canada First Research Excellence Fund (CFREF), as well as the University of Alberta Faculty of Science and Faculty of Graduate Studies. N.L., R.G., W.C., S.L., and J. Z. acknowledge the China Scholarship Council (CSC). The authors thank Roy Schaffrinna, Shanshan Yin, and Baohui Chen for sample preparations. The authors thank Julija Reitenbach and Simon J. Schaper for the SE measurement and analysis. The authors thank Prof. Alexander Holleitner and Peter Weiser for providing access to the SEM. The GISAXS measurements were performed at the third-generation synchrotron source PETRA III at DESY in Hamburg, Germany, a member of the Helmholtz Association (HGF).

Open access funding enabled and organized by Projekt DEAL.

Conflict of Interest

The authors declare no conflict of interest.

Data Availability Statement

Data available on request from the authors.

Keywords

enhanced electron transfer, germanium nanocrystals, ordered mesoporous nanostructures, photoanodes, titania

Received: March 2, 2021
Revised: May 12, 2021
Published online: June 17, 2021

[1] K. Lan, R. Wang, Q. Wei, Y. Wang, A. Hong, P. Feng, D. Zhao, *Angew. Chem., Int. Ed.* **2020**, *59*, 2.
[2] H. Liu, W. Li, D. Shen, D. Zhao, G. Wang, *J. Am. Chem. Soc.* **2015**, *137*, 13161.
[3] C. Yi, X. Li, J. Luo, S. M. Zakeeruddin, M. Grätzel, *Adv. Mater.* **2016**, *28*, 2964.
[4] S. Ito, P. Chen, P. Comte, M. K. Nazeeruddin, P. Liska, P. Péchy, M. Grätzel, *Prog. Photovoltaics* **2007**, *15*, 603.
[5] B. O'Regan, M. Grätzel, *Nature* **1991**, *353*, 737.
[6] M. Gao, L. Zhu, W. L. Ong, J. Wang, G. W. Ho, *Catal. Sci. Technol.* **2015**, *5*, 4703.
[7] Y. Bai, I. Mora-Seró, F. De Angelis, J. Bisquert, P. Wang, *Chem. Rev.* **2014**, *114*, 10095.
[8] S. R. Gajjela, K. Ananthanarayanan, C. Yap, M. Grätzel, P. Balaya, *Energy Environ. Sci.* **2010**, *3*, 838.
[9] H. Liu, J. Tang, I. J. Kramer, R. Debnath, G. I. Koleilat, X. Wang, A. Fisher, R. Li, L. Brzozowski, L. Levina, E. H. Sargent, *Adv. Mater.* **2011**, *23*, 3832.
[10] X. Li, M. I. Dar, C. Yi, J. Luo, M. Tschumi, S. M. Zakeeruddin, M. K. Nazeeruddin, H. Han, M. Grätzel, *Nat. Chem.* **2015**, *7*, 703.
[11] A. Yella, H.-W. Lee, H. N. Tsao, C. Yi, A. K. Chandiran, M. K. Nazeeruddin, E. W.-G. Diau, C.-Y. Yeh, S. M. Zakeeruddin, M. Grätzel, *Science* **2011**, *334*, 629.
[12] W. S. Yang, J. H. Noh, N. J. Jeon, Y. C. Kim, S. Ryu, J. Seo, S. Il Seok, *Science* **2015**, *348*, 1234.
[13] H. Nagaoka, F. Ma, D. W. Dequilettes, S. M. Vorpahl, M. S. Glaz, A. E. Colbert, M. E. Ziffer, D. S. Ginger, *J. Phys. Chem. Lett.* **2015**, *6*, 669.
[14] H. Zhou, Q. Chen, G. Li, S. Luo, T. Song, H.-S. Duan, Z. Hong, J. You, Y. Liu, Y. Yang, *Science* **2014**, *345*, 542 LP.
[15] D. Wang, Y. L. Chang, Q. Wang, J. Cao, D. B. Farmer, R. G. Gordon, H. Dai, *J. Am. Chem. Soc.* **2004**, *126*, 11602.
[16] K. A. Mengle, S. Chae, E. Kioupakis, *J. Appl. Phys.* **2019**, *126*, 85703.
[17] H. P. Wu, J. F. Liu, M. Y. Ge, L. Niu, Y. W. Zeng, Y. W. Wang, G. L. Lv, L. N. Wang, G. Q. Zhang, J. Z. Jiang, *Chem. Mater.* **2006**, *18*, 1817.
[18] M. M. Bentlohner, M. Waibel, P. Zeller, K. Sarkar, P. Müller-Buschbaum, D. Fattakhova-Rohlfing, T. F. Fässler, *Angew. Chem., Int. Ed* **2016**, *55*, 2441.
[19] Y. Duan, Q. Tang, Z. Chen, B. He, H. Chen, *J. Mater. Chem. A* **2014**, *2*, 12459.
[20] A. Kitiyanan, T. Kato, Y. Suzuki, S. Yoshikawa, *J. Photochem. Photobiol., A* **2006**, *179*, 130.
[21] S. Chatterjee, *J. Phys. D: Appl. Phys.* **2008**, *41*, 55301.
[22] M. S. Ahmad, A. K. Pandey, N. A. Rahim, *IOP Conf. Ser: Mater. Sci. Eng.* **2018**, *358*, 12015.
[23] A. F. Khan, M. Mehmood, T. Ali, H. Fayaz, *Thin Solid Films* **2013**, *536*, 220.
[24] J. Gutierrez, A. Tercjak, I. Mondragon, *J. Am. Chem. Soc.* **2010**, *132*, 873.
[25] N. Li, L. Song, L. Bießmann, S. Xia, W. Ohm, C. J. Brett, E. Hadjixenophontos, G. Schmitz, S. V. Roth, P. Müller-Buschbaum, *Adv. Mater. Interfaces* **2019**, *6*, 1900558.
[26] L. Song, A. Abdelsamie, C. J. Schaffer, V. Körstgens, W. Wang, T. Wang, E. D. Indari, T. Fröschl, N. Hüsing, T. Haeberle, P. Lugli, S. Bernstorff, P. Müller-Buschbaum, *Adv. Funct. Mater.* **2016**, *26*, 7084.
[27] A. G. Tomulescu, V. Stancu, C. Beşleagă, M. Enculescu, G. A. Nemneş, M. Florea, V. Dumitru, L. Pintilie, I. Pintilie, L. Leonat, *Energy Technol.* **2020**, *8*, 1900922.
[28] H. Tang, K. Prasad, R. Sanjines, P. E. Schmid, F. Levy, *J. Appl. Phys.* **1994**, *75*, 2042.
[29] J. N. L. Albert, T. H. Epps, *Mater. Today* **2010**, *13*, 24.
[30] M. Javadi, V. K. Michaelis, J. G. C. Veinot, *J. Phys. Chem. C* **2018**, *122*, 17518.
[31] S. Xia, L. Song, N. Hohn, K. Wang, S. Grott, M. Opel, M. Schwartzkopf, S. V. Roth, P. Müller-Buschbaum, *Adv. Funct. Mater.* **2019**, *29*, 1808427.
[32] C. H. Lee, T. Nishimura, K. Nagashio, K. Kita, A. Toriumi, *IEEE Trans. Electron Devices* **2011**, *58*, 1295.
[33] N. Li, W. Chen, L. Song, R. Guo, M. A. Scheel, D. Yang, V. Körstgens, M. Schwartzkopf, S. V. Roth, P. Müller-Buschbaum, *ACS Appl. Mater. Interfaces* **2020**, *12*, 57627.
[34] S. Xia, L. Song, W. Chen, V. Ko, M. Opel, M. Schwartzkopf, S. V. Roth, P. Müller-Buschbaum, *ACS Appl. Mater. Interfaces* **2019**, *11*, 21935.
[35] Q. Ma, T. P. Qin, S. J. Liu, L. Q. Weng, W. Y. Dong, *Appl. Phys. A* **2011**, *104*, 365.
[36] K. Wang, V. Körstgens, D. Yang, N. Hohn, S. V. Roth, P. Müller-Buschbaum, *J. Mater. Chem. A* **2018**, *6*, 4405.
[37] G. H. Vineyard, *Phys. Rev. B* **1982**, *26*, 4146.
[38] S. K. Sinha, E. B. Sirota, S. Garoff, *Phys. Rev. B* **1988**, *38*, 2297.
[39] M. Rauscher, T. Salditt, H. Spohn, *Phys. Rev. B* **1995**, *52*, 16855.
[40] R. Lazzari, *J. Appl. Crystallogr.* **2002**, *35*, 406.
[41] N. Li, L. Song, N. Hohn, N. Saxena, W. Cao, X. Jiang, P. Müller-Buschbaum, *Nanoscale* **2020**, *12*, 4085.
[42] L. Song, M. Rawolle, N. Hohn, J. S. Gutmann, H. Frielinghaus, P. Müller-Buschbaum, *Small* **2018**, *14*, 1801461.

[43] S. Xia, L. Song, M. Schwartzkopf, V. Körstgens, S. V. Roth, P. Müller-Buschbaum, *Nanoscale* **2018**, *10*, 11930.
[44] L. Song, W. Wang, V. Körstgens, D. Moseguí González, F. C. Löhrer, C. J. Schaffer, J. Schlipf, K. Peters, T. Bein, D. Fattakhova-Rohlfing, S. V. Roth, P. Müller-Buschbaum, *Nano Energy* **2017**, *40*, 317.
[45] X. Y. Wang, Z. L. Xue, J. L. Li, *J. South Afr. Inst. Min. Metall.* **2016**, *116*, 1159.
[46] N. M. Al-Hada, E. B. Saion, A. H. Shaari, M. A. Kamarudin, M. H. Flaifel, S. H. Ahmad, S. A. Gene, *PLoS One* **2014**, *9*, 2.
[47] L. Song, W. Wang, V. Körstgens, D. Moseguí González, Y. Yao, N. K. Minar, J. M. Feckl, K. Peters, T. Bein, D. Fattakhova-Rohlfing, G. Santoro, S. V. Roth, P. Müller-Buschbaum, *Adv. Funct. Mater.* **2016**, *26*, 1498.
[48] Y. Son, M. Park, Y. Son, J. Lee, J. Jang, Y. Kim, J. Cho, *Nano Lett.* **2014**, *14*, 1005.
[49] M. Javadi, D. Picard, R. Sinelnikov, M. A. Narreto, F. A. Hegmann, J. G. C. Veinot, *Langmuir* **2017**, *33*, 8757.
[50] N. Hohn, A. E. Hetzenecker, M. A. Giebel, S. Geier, L. Bießmann, V. Körstgens, N. Saxena, J. Schlipf, W. Ohm, P. S. Deimel, F. Allegretti, J. V. Barth, S. V. Roth, T. F. Fässler, P. Müller-Buschbaum, *Nanoscale* **2019**, *11*, 2048.
[51] J. Zhao, L. Yang, J. A. McLeod, L. Liu, *Sci. Rep.* **2015**, *5*, 17779.
[52] X. H. Sun, C. Didychuk, T. K. Sham, N. B. Wong, *Nanotechnology* **2006**, *17*, 2925.
[53] A. C. M. Esther, A. Dey, N. Sridhara, B. Yougandar, P. Bera, C. Anandan, D. Rangappa, A. K. Sharma, *Surf. Interface Anal.* **2015**, *47*, 1155.
[54] K. Prabhakaran, T. Ogino, *Surf. Sci.* **1995**, *325*, 263.
[55] K. Prabhakaran, F. Maeda, Y. Watanabe, T. Ogino, *Thin Solid Films* **2000**, *369*, 289.
[56] W. L. Jolly, W. M. Latimer, *J. Am. Chem. Soc.* **1952**, *74*, 5757.
[57] S. Golczak, A. Kanciurzewska, M. Fahlman, K. Langer, J. J. Langer, *Solid State Ionics* **2008**, *179*, 2234.
[58] C. V. Ramana, R. J. Smith, O. M. Hussain, *Phys. Status Solidi A* **2003**, *199*, R4.
[59] L. K. Reb, M. Böhmer, B. Predeschly, S. Grott, C. L. Weindl, G. I. Ivandekic, R. Guo, C. Dreißigacker, R. Gernhäuser, A. Meyer, P. Müller-Buschbaum, *Joule* **2020**, *4*, 1880.
[60] Q. Jiang, Z. Chu, P. Wang, X. Yang, H. Liu, Y. Wang, Z. Yin, J. Wu, X. Zhang, J. You, *Adv. Mater.* **2017**, *29*, 1.
[61] D. Yang, R. Yang, K. Wang, C. Wu, X. Zhu, J. Feng, X. Ren, G. Fang, S. Priya, S. (Frank) Liu, *Nat. Commun.* **2018**, *9*, 3239.
[62] X. Sun, J. Xu, L. Xiao, J. Chen, B. Zhang, J. Yao, S. Dai, *Int. J. Photoenergy* **2017**, *2017*, 1.
[63] Y. Li, L. Meng, Y. Yang, G. Xu, Z. Hong, Q. Chen, J. You, G. Li, Y. Yang, Y. Li, *Nat. Commun.* **2016**, *7*, 10214.
[64] N. Kholmicheva, P. Moroz, H. Eckard, G. Jensen, M. Zamkov, *ACS Energy Lett.* **2017**, *2*, 154.
[65] P. W. Liang, C. Y. Liao, C. C. Chueh, F. Zuo, S. T. Williams, X. K. Xin, J. Lin, A. K. Y. Jen, *Adv. Mater.* **2014**, *26*, 3748.
[66] A. Buffet, A. Rothkirch, R. Döhrmann, V. Körstgens, M. M. Abul Kashem, J. Perlich, G. Herzog, M. Schwartzkopf, R. Gehrke, P. Müller-Buschbaum, S. V. Roth, *J. Synchrotron Radiat.* **2012**, *19*, 647.